

**Pollutant Dispersion in a Large Indoor Space :**

**Part 1 – Scaled experiments using a water-filled model with occupants and furniture**

T. L. Thatcher<sup>1,\*</sup>, D.J. Wilson<sup>2</sup>, E.E. Wood<sup>1</sup>, M.J. Craig<sup>1</sup>, and R.G. Sextro<sup>1</sup>

<sup>1</sup>Lawrence Berkeley National Laboratory,

1 Cyclotron Road MS 90R3058

Berkeley, CA 94720. USA

<sup>2</sup>Dept. of Mechanical. Engineering

University of Alberta

Edmonton, Canada

---

\* Corresponding author: 510-486-5215, FAX 510-486-6658, tlthatcher@lbl.gov

## Abstract

Scale modeling is a useful tool for analyzing complex indoor spaces. Scale model experiments can reduce experimental costs, improve control of flow and temperature conditions, and provide a practical method for pre-testing full-scale system modifications. However, changes in physical scale and working fluid (air or water) can complicate interpretation of the equivalent effects in the full-scale structure. This paper presents theoretical and experimental results of scale modeling. Theoretical calculations are derived for predicting the effects from losses of molecular diffusion, small scale eddies, turbulent kinetic energy, and turbulent mass diffusivity in a scale model, even without Reynolds number matching. Pollutant dispersion experiments were performed in a water-filled 30:1 scale model of a large room, using uranine dye injected continuously from a small point source. Pollutant concentrations were measured in a plane, using laser induced fluorescence techniques, for three interior configurations: unobstructed, table-like obstructions, and table-like and figure-like obstructions. Concentrations within the measurement plane varied by more than an order of magnitude, even after the concentration profile was fully developed. Objects in the model interior had a significant effect of both the concentration profile and fluctuation intensity in the measurement plane.

**Keywords:** Scaling rules, contaminant transport, indoor air quality, turbulence, laser induced fluorescence.

## 1. Introduction

Point source pollutant releases in the indoor environment arise from a variety of sources, from leaky equipment to spilled chemicals. When planning for and responding to

these types of emergencies, the action required will depend not only on the average pollutant concentration but also on the concentration distribution within the source room. For instance, making planning decisions, such as optimal chemical sensors locations or evacuation routes least likely to increase exposure, requires an understanding of pollutant movement within the room. For large indoor spaces, such as an auditorium or atrium, it is unrealistic to assume that the pollutant concentration will become well-mixed quickly.

For applications where the rapid, well-mixed assumption is inadequate, some researchers, such as Drescher, et al. (1995) and Baughman, et al. (1994), used the concept of mixing time to describe the time it takes for an instantaneous release into an unventilated space to become well-mixed. While this method has many useful applications, it does not work well for continuous releases or in a mechanically ventilated space since concentrations may never become well-mixed under these conditions. Additionally, the mixing-time concept cannot be used to describe the concentration profiles during the mixing phase.

Predicting the time-dependent pollutant concentration profile from a suddenly started or pulsed point source in a large room is one of the most difficult problems in turbulent mixing. Turbulent airflows inside a ventilated room produce a pollution cloud that is diluted at first by the fresh room air and later by contaminated air returned by the large scale turbulent circulation patterns.

The smaller the source diameter relative to the turbulent eddies in the room air, the more the plume centroid will meander as it mixes with room air (see Wilson, 1995 for more details). This means that, even when all conditions are held constant, there will be large variations in concentration, in both time and space, between independent releases.

Useful predictions require a series of identical, independent experiments to determine not only the mean concentration for each location as a function of time, but also the concentration variability, which is characterized by the fluctuation intensity for each point in space. Computational fluid dynamics models and/or large eddy simulation models can be used to predict pollutant concentrations under these conditions. However, due to the inherent complexity of the problem, confidence in the model results requires comparisons against experimental data with high spatial and temporal resolution.

Since obtaining a high degree of spatial and temporal resolution in a full-scale experiment is difficult, scale models are useful for providing information about flow and concentration profiles in a larger space. For example, Huber, et al. (1991) used video imaging of smoke in a wind tunnel to investigate dispersion in the wake of a model building. Hunt and Linden (1999) and Hunt, et al (2001) used water-filled models and saline fluid to investigate the effect of buoyancy differentials on flow patterns within a rectangular enclosure. The US Department of Transportation (1975) studied subway tunnels and stations using both pressurized and non-pressurized models to explore the affects of train motion on airflow. They also investigated scaling effects due to boundary layer thickness using both theory and experiments. More recently, Bain (2001) performed tests in a detailed scale model of a subway station for both airflow rates and smoke dispersion. In the fluid mechanics literature, many researchers have used flow visualization techniques in general (e.g. Hesselink, 1988; Freymuth, 1993) and laser induced fluorescence (LIF) techniques in particular (e.g. Walker, 1987; Arcoumanis et al, 1990). LIF has been used to investigate fluid mechanics problems ranging from impinging jets to nuclear reactor coolant systems (Koochesfahani and Dimotakis, 1985; Shlien, 1988;

Lemoine et al, 1998; Unger and Muzzio, 1999; Gavelli and Kiger, 2000; Crimaldi and Koseff, 2001)

In this study, we use LIF techniques to simulate turbulent air mixing and point source dispersion using a small-scale (30:1) water-filled physical model of a large room including HVAC system airflows. The room being modeled is a large experimental chamber (7m  $\times$  9m  $\times$  11m) at the Lawrence Berkeley National Laboratory. The full-scale experimental chamber is used for investigating pollutant dispersion in tall indoor spaces, such as atriums and auditoriums. We develop analytical methods for predicting the quantitative effects of a mismatch in Reynolds numbers for scale-model and full sized room and supply jet. As we discuss later, there are significant advantages in performing scale-model experiments to understand pollutant dispersion in large spaces.

Our study will focus on mixing by room turbulence of a small neutrally buoyant source created by the mean kinetic energy of the supply air jets, and by obstacles such as furniture and people. In this purely isothermal situation, we do not consider the important complications that arise from positive or negative buoyancy in the supply air, in the source gas or aerosol, from heat generation by occupants, or from heating by temperature differences between the room surfaces and the room air. Our objective, in the addition to exploring the use of a water-filled scale model, is to obtain high-resolution data for comparison with results from a computational fluid dynamics model, as described by Finlayson et al, 2003.

## 2. Scale Modeling of Room Turbulence and Contaminant Dispersion

Ideally, scale model results will match full scale room results exactly. Choosing experimental conditions that provide exact matching requires an understanding of the factors affecting turbulence in the full scale, air-filled room and in the water-filled scale model. For these experiments, only mechanical flow effects are investigated, with neutrally buoyant emission from the point source of pollution dispersing in isothermal room air. Under these conditions, the structure of the largest eddies in the turbulence velocity field are determined by the mechanically generated turbulence produced in the mean velocity field by the ventilation supply jets.

In any mixing process, the dynamics of the smallest turbulent eddies are determined by the rate at which turbulence energy is being removed by viscous dissipation. For mechanical turbulence, the geometric similarity of the model and full-scale room, as well as the ventilation inlets and outlets, must be maintained. Furthermore, the Reynolds number of the inlet supply jets must be equal in the model and at full scale. Reynolds number matching is required to maintain the same range of turbulent eddy sizes in the model and full-scale rooms. Additionally, the time scaling factor linking the mixing rate in the model and full scale must be calculated to transform time-dependent processes from model to full scale.

Matching model and full-scale processes requires definitions of length, velocity, and time scales for both the inlet supply jets and the room flow patterns driven by these jets. We define these scales based on the physical dimensions and flow rates:

### Mean Length Scales Mean Velocity Scales

$$S_{\text{inlet}} \equiv A_{\text{inlet}}^{1/2}$$

$$U_{\text{inlet}} \equiv Q_{\text{inlet}}/A_{\text{inlet}}$$

### Residence Times

$$t_{\text{inlet}} \equiv A_{\text{inlet}}^{3/2}/Q_{\text{inlet}}$$

$$S_{\text{room}} \equiv V_{\text{room}}^{1/3} \quad U_{\text{room}} \equiv Q_{\text{inlet}}/V_{\text{room}}^{2/3} \quad t_{\text{room}} \equiv V_{\text{room}}/Q_{\text{inlet}}$$

$$\text{Re}_{\text{inlet}} = \frac{U_{\text{inlet}} S_{\text{inlet}}}{\nu_{\text{inlet}}} = \frac{Q_{\text{inlet}}}{A_{\text{inlet}}^{1/2} \nu_{\text{inlet}}}$$

$$\text{Re}_{\text{room}} = \frac{U_{\text{room}} S_{\text{room}}}{\nu_{\text{room}}} = \frac{Q_{\text{inlet}}}{V_{\text{room}}^{1/3} \nu_{\text{room}}}$$

Based on these definitions, the two mean flow Reynolds numbers can be defined,

where  $\nu_{\text{inlet}}$  and  $\nu_{\text{room}}$  are the kinematic viscosities,  $\text{m}^2 \text{s}^{-1}$ , for the fluids: water in the scale model and air in the full scale room.

### 2.1 Scale Modeling with Matched Reynolds Numbers

For a perfect match, both the inlet and room Reynolds numbers in the model should

$$\frac{Q_{\text{inlet, full}}}{A_{\text{inlet, full}}^{1/2} \nu_{\text{air}}} = \frac{Q_{\text{inlet, model}}}{A_{\text{inlet, model}}^{1/2} \nu_{\text{water}}}$$

be the same as in the full scale room. For the inlet jets, this condition is met if:

For the room flow this condition is met if:

$$\frac{Q_{\text{inlet, full}}}{V_{\text{room, full}}^{1/3} \nu_{\text{air}}} = \frac{Q_{\text{inlet, model}}}{V_{\text{room, model}}^{1/3} \nu_{\text{water}}}$$

If the defined length and velocity scales are substituted into these equations then both equations become:

$$\frac{Q_{inlet, full}}{Q_{inlet, model}} = \left( \frac{S_{full}}{S_{model}} \right) \left( \frac{\nu_{air}}{\nu_{water}} \right)$$

For a model where the room and inlets are scaled by the same factor, a solution for Reynolds number matching of the inlet will also match the Reynolds number for room flow under mechanically driven flow conditions. This equation can be solved knowing that the ratio of the kinematic viscosities of air to water is approximately 11.66 and the ratio of the length scales in these experiments is 30. Perfect matching of the room and inlet Reynolds numbers occurs when the volumetric flow rate in the full-scale room is 350 times that in the model.

The time scale for Reynolds number matching can be determined from the time scale definitions as:

$$\frac{t_{room, full}}{t_{room, model}} = \frac{\left( \frac{V_{room, full}}{Q_{inlet, full}} \right)}{\left( \frac{V_{room, model}}{Q_{inlet, model}} \right)} = \left( \frac{S_{room, full}}{S_{room, model}} \right)^3 \left( \frac{Q_{inlet, model}}{Q_{inlet, full}} \right)$$

For our 30:1 scale model with a flow rate ratio of 350, the time scale ratio from this equation is 77, meaning one second in the model would simulate 77 seconds in the full scale room. In the full-scale room being modeled in these experiments, the air exchange rate is 4 air changes per hour. Consequently, Reynolds number matching occurs when the model operates at  $308 \text{ h}^{-1}$  or one volume change every 11.7 seconds. For our 27.8  $\ell$  water tank, this results in a water flow rate of about  $150 \text{ l m}^{-1}$ .

Although it would be possible to operate the water model at these high flow rates, several factors complicate the process. These flow rates and the pressures developed within the model would require large pumps, significant structural reinforcement, and a

large capacity water storage system. In addition, a high speed image acquisition system would have been required for capturing the data at the 77:1 time speedup required for perfect Reynolds number matching.

Fortunately, as we will show in the next section, turbulence theory predicts that under fully turbulent flow conditions reducing the model Reynolds number is likely to have only a small effect on the correlation between the model and full-scale results. Given the difficulties in operating the model with an exact Reynolds number match, we chose to run the model at a lower flow rate, resulting in a Reynolds number that was reduced but still produced well-developed turbulent flow.

## *2.2 Scale Modeling with Unequal Reynolds Numbers*

Ideally, a scale model would exactly match the Reynolds numbers for the larger space being emulated. In practice, this is usually quite difficult to achieve when the geometric scale of the model is smaller than about 1:10. When model and full scale Reynolds numbers do not match exactly, it is possible to use turbulence theory to estimate how the model and full-scale results differ. The Reynolds number dependence of turbulence length and velocity scales allows quantitative estimation of the loss of small eddy sizes and the fraction of turbulence kinetic energy lost in the scaled-up model. The effects on turbulent eddy diffusivities of concentration and velocity and the flow in the inlet jets and jet-driven turbulence can also be estimated.

If the Reynolds number in the small-scale model is still high enough for an inertial subrange of eddy sizes to exist, then the equations developed in Appendix B can be used to estimate the Reynolds number effects on room turbulence. As shown in Figure 1, the

inertial subrange consists of the range of eddy sizes that are too small to be active in the production of turbulence from the velocity shear in the jets and too large to be active in the viscous dissipation of turbulence. Inertial subrange eddies control the rate of turbulence energy transport from the large production scales to the active dissipation scales and allow us to relate the size of the largest turbulence scales (the room size) to the size of the dissipation scales that are affected by changes in Reynolds number. The theory of turbulence production and dissipation, as well as inertial subrange properties, is described in more detail by Tennekes and Lumley (1971) and Hinze (1975).

The difference in the Reynolds number for the scale model leads to difference in the turbulence characteristics. In Appendix B we develop analytical methods for determining the effects on the three most important turbulence characteristic: (1) size of the smallest eddy, (2) turbulent kinetic energy, and (3) turbulent mass diffusivity.

The smallest eddies in the full scale room air were calculated to be  $\eta_{\text{room,full}} = 0.38$  cm and the smallest eddies in the water model were  $\eta_{\text{room,model}} = 0.032$  cm. Multiplying by 30 to scale up the water model eddies to their equivalent full scale size gives a value of  $\eta_{\text{room,scaleup}} = 0.97$  cm. Velocity eddies between the actual Kolomorgov scale of 0.38 cm in the full scale room air and the scaled-up model value of 0.97 cm were not simulated in the water experiments. The difference caused by loss of the smallest eddies in the scale model is unlikely to be apparent in the processed video images. One reason for this is that the effective spatial resolution of the images was equivalent to 0.3 x 0.3 cm in the model (9x9 cm in full scale). This video image resolution masked the loss of the smallest scale eddies (0.032 cm) in the model. As a consequence, the lower model Reynolds number in our experiments had no visible effect on the recorded images. If significantly higher resolution

imaging was used, the loss of the smallest eddies in the scale model would result in slightly more blurred plume edges than would be seen in full scale.

The effects on turbulent kinetic energy and mass diffusivity are also very subtle. The model results in a 2% loss of the turbulence kinetic energy or 1% of the turbulent scaling velocity. Similarly, the ratio of scaled-up model to full scale room turbulent mass diffusivities (0.96) results in a very minor effect. Both of these scaling effects are smaller significant than the uncertainties associated with the experiments. For instance, the water flow rate in the scale model had an uncertainty of  $\pm 3\%$ .

The largest source of uncertainty is that Reynolds number effects may cause the modeled turbulence to be more or less anisotropic than the full-scale flow, and this change in flow anisotropy could have a significant effect on turbulent diffusivities in the x, y and z directions. We have no quantitative way of estimating the importance of changing anisotropy on the scale model dispersion.

### **3. Choosing an Operating Fluid and Scaling Ratio**

The choice of operating fluid (typically air or water) will affect how well the scale model represents the full-scale turbulence. Since the ratio of the kinematic viscosities of air to water is approximately 11.66, the two fluids will have very different Reynolds numbers under the same flow conditions. Moreover, the choice of operating fluid will determine the range of flow detection techniques available. Some flow detection techniques are better suited to water models, such as dye or salt, while others are better suited to air, such as smoke.

Scaling ratio is also a critical factor in determining how well a model represents the physical system. Larger models have turbulence characteristics that more closely match those of the full-scale system. However, the benefits of scaling in terms of ease of model construction and operation are reduced as the model becomes larger.

For identical Reynolds numbers, the turbulence characteristics are perfectly matched. However, shifts in time and flow scales may make model operation difficult. Table 1a gives model/full size ratios for important model parameters with exact Reynolds number matching. For smaller air-filled models, the time scale ratios become large, requiring rapid data collection. For instance, in a 30:1 scale air-filled model the equivalent of one hour of flow development in the full scale room occurs in 4 seconds within the scale model. In this case, a sample frequency of 15 hz would capture the equivalent of one image per minute of full scale flow development. In addition, for a typical commercial office air register velocity of  $6.3 \text{ m s}^{-1}$  (1250 ft per minute), the air model requires a face velocity of  $190 \text{ m s}^{-1}$  or over half the speed of sound. In contrast, if the same 30:1 model is filled with water, the equivalent sample frequency and inlet velocity are each reduced by more than an order of magnitude.

Table 1b shows properties of the full-scale system and several model scales in air and water for a time scale ratio set at 15:1 (model : full). This time ratio was chosen to illustrate the effects of physical scale and fluid choices. Other time scales could be used, depending on the interests of a particular experiment. Due to the differences between physical properties of water and air, a small water-filled model can match the turbulence characteristics of the full-scale room more closely than an air-filled model operated at the same flow rates. For instance, using air rather than water in a 30:1 scale model decreases

the model Reynolds number by over 90%, greatly increasing the errors from Reynolds number mismatch between model and full-scale rooms. Consequently, the smallest eddy size increases by more than a factor of 6 and the ratio of turbulent mass diffusivities in air is about half that in water. The importance of operating fluid choice is best demonstrated by comparing a 30:1 water filled model with a 10:1 air filled model. Although the water filled model is significantly smaller, it matches the turbulence characteristic of the full-scale system slightly better than the air filled model.

The choice of physical model scale, operating fluid, and time scale will be determined by the experimental objectives of any given set of experiments. Considerations such as the required spatial and time resolution, as well as the desired flow detection technique and achievable data collection rate, will govern the decisions made.

#### **4. Experimental Methods**

A 30:1 scale water-filled model of the Lawrence Berkeley National Laboratory Large-scale Indoor Facility for Tracer Gas Experiments (LIFTGE) was constructed to investigate indoor air pollutant dispersion from point sources. A description of the LIFTGE, along with initial tracer gas results is presented in Fischer, et al (2001).

A schematic of the model is shown in Figure 2. Water was used to simulate the supply inlet and room fluid flows. The water model was built using a 75 liter glass tank divided with a partition. One side of the partition defined the 30:1 scale model, with an internal volume of 27.8 liters, while the other side provided a container into which the room exhaust passed through an overflow weir simulating a ceiling-level exhaust duct in the full-scale room. The upper surface of the model room was a free water surface, rather

than a solid ceiling. This free surface allowed the video camera to record dispersion without interference from the accumulation of air bubbles that would have built up under an otherwise transparent ceiling plate.

The pollutant release was simulated by injecting uranine (disodium fluorescein) dye solution into the scale-model tank just above the floor at the position shown in Figure 2. Dye solution, with a uranine mass concentration of  $10 \text{ mg L}^{-1}$ , was released from the porous surface of a 0.5 cm diameter plastic foam ball at a steady release rate of  $1.0 \text{ cm}^3 \text{ s}^{-1}$  controlled by a peristaltic pump. This emission rate produced a source velocity of about  $1.3 \text{ cm s}^{-1}$ . The low molecular diffusivity of fluorescein dye into water is a reasonable approximation of the dispersion of a small particle aerosol into room air, as can be seen by comparing the molecular Schmidt number,  $Sc$ . Fluorescein dispersion into water has a  $Sc \sim 10^3$ , similar to the Schmidt number for 0.02 micrometer diameter particles dispersed in air. The 'smearing-out' effect of turbulent dispersion eddies by molecular diffusion is important only for Schmidt numbers of order unity, so effects from differences in Schmidt numbers should be insignificant.

To begin each experiment, the model room was filled with fresh, dye-free water. The model was then ventilated by fresh water that flowed through 5 water inlets placed to approximate the air supply inlets in the full-scale room (30:1 scaled-down rectangular orifices). All experiments were conducted in a single pass configuration (with no recirculation of contaminated water from the overflow outlet back to the inlets). The total ventilation flow rate was  $28 \text{ L m}^{-1}$ , or  $1.0 \text{ min}^{-1}$ . The model volume exchange rate was 15 times larger than the full-scale air exchange rate of  $4.0 \text{ h}^{-1}$ , making 1 second in the model equivalent to 15 seconds in the full-scale room.

A horizontal sheet of blue-green light approximately 3 mm thick and centered 6 cm from the floor of the water model was formed by using a cylindrical lens to spread the beam from a 5 watt, argon-ion laser (Spectra Physics, model 168). At 30:1 scale, this sheet-lighted plane was approximately at the equivalent breathing zone in the full-sized room. The incoming laser light causes the fluorescein dye to fluoresce at a different wavelength than the several wavelengths being emitted in the multi-mode laser beam. A selective light filter (Kodak Wratten 15) prevented scattered or reflected laser light from reaching the camera, meaning essentially only light emitted by dye fluorescence was measured.

A monochrome video camera (Hitachi, KP-M1) with analog composite NTSC output (standard North American TV video) was mounted directly above the tank to record the fluorescence emitted from the laser-illuminated plane. For fluorescein, the dye fluorescence intensity emitted at each pixel location is directly proportional to the product of the local dye concentration and the local intensity of the laser light (see Walker 1987). The intensity output from our camera responded linearly to changes in light intensity, allowing the use of a linear calibration scale to convert camera output to dye concentration. Because the laser excitation wavelength for the dye was different than the wavelength of the emitted fluorescence, the unexcited dye in the region above the measurement plane did not attenuate the light that reached the camera. Consequently, no attenuation correction was needed along the vertical path from the excitation light sheet to the video camera.

Camera images were digitized using a personal computer connected to an NTSC composite video capture board (GrabIt Pro, Aims Laboratory) capable of recording high resolution still images at 1 frame per second or lower resolution images at 5 frames per

second. Calibration images were recorded with no dye present and with well mixed concentrations of fluorescein dye.

The digitized images were analyzed by an image processing program (Scion Image, Scion Corporation) where they were cropped and the background count levels were subtracted from each pixel. Since the light intensity in the plane was not uniform, a flat field correction was performed by dividing the measured intensity at each pixel in the image by the measured intensity at the same pixel obtained from an image of uniform dye concentration. The images were then smoothed digitally to reduce the effect of camera noise by replacing the value at the center pixel in a 5 pixel by 5 pixel square with the average of those 25 pixels. The average light intensities for several different well-mixed concentrations of fluorescein dye were used to produce a calibration curve. The fluorescence intensity of the corrected images was linear over the concentration range measured in the experiments.

## **5. Measurements of Contaminant Concentration Profiles using the Water-filled Model**

Three different interior configurations were used for these experiments. In the first configuration, the interior of the model was unobstructed, containing only the dye source and a small tube running along the floor connected to the peristaltic injection pump. In the second configuration, five obstructions representing rows of tables were placed on the floor of the model in parallel rows. For the third configuration, twelve obstructions with the approximate dimensions of standing human adults were placed on the model floor in addition to the table-like obstructions. The tops of the human-like obstructions were just

below the measurement plane, so that the laser light was not obstructed by the figures. The human-like obstructions were not heated and consequently do not simulate the effect of the thermal plumes caused by real people. A schematic of the obstructions is shown in Figure 3. An overhead view of the layout of these obstructions within the model is shown in Figure 4.

Experiments were performed to investigate dye concentrations in the measurement plane under both transient and fully developed conditions. Water flow was initiated at least 3 minutes before any dye was injected (3 volumes of flow). This established a fully developed flow field prior to dye injection. Since each run represents only one realization of a highly variable stochastic process, capturing a statistical representation of the developing flow requires multiple runs for a given set of flow conditions. In these experiments, we typically captured 20 replicate runs for both 5-frame-per-second lower resolution and 1-frame-per-second higher resolution images. Each of these experiments captured approximately 1000 sequential images.

For experiments with fully developed concentration profiles, dye injection was initiated 5 minutes prior to initiating image collection. Then, one image was collected every 3 seconds for 50 minutes (1000 images). “Average concentration” images show the average value at each pixel for a given set of data. “Fluctuation intensity” images represent the standard deviation of the values at each pixel divided by the average concentration at that pixel. Comparisons between replicate sets of images show that 1000 images provide enough independent profiles to characterize the concentration and fluctuations repeatably.

## 6. Discussion of Water-filled Model Results

Results from the transient experiments in the unobstructed model are shown in Figure 5. The images are shown for 1 second intervals starting 6 seconds after the initiation of dye discharge. Each image in Figure 5 represents the average of 19 concentration images, each from a different run, taken at the same elapsed time after the start of dye injection. Averaging the frames reduces the effect of stochastic run-to-run variability and demonstrates the evolution of the average concentration in the image plane. Dye first appears in the image plane approximately 5 seconds after dye flow starts (equivalent to 75 seconds full-scale). In addition to growth of the plume with time, consecutive frames (e.g. 9 and 10 seconds) also show fluctuations, indicating there were an insufficient number of replicates to obtain well defined profiles for the developing flow. However, the replicates are sufficient in number to provide a reasonable sense of the time evolving average concentration profile. The transient concentration averages for the measurement plane are compared to those predicted by a computational fluid dynamics model by Finlayson et al. (2003).

Even after the concentration distribution becomes fully established, the stochastic nature of the flow leads to large changes in the instantaneous concentration profile in the measurement plane over time. However, the time-averaged concentration profile remains stable. To obtain meaningful time-average concentration profiles, a large number of independent images needs to be averaged. Figure 6 illustrates this point by comparing pairs of concentration profiles obtained for single images and those obtained by averaging 5, 10, and 200 images for a fully developed concentration profile in the unobstructed model. Each of the two average images was obtained using different independent sets of

frames from a single experiment. When a small number of frames was averaged, the concentration profile was dependent on which frames were used for the average, as can be seen by the large variation between the pairs of images shown in (a) and (b). As a larger number of frames was used, the averages converge to a consistent image of the concentration profile, as shown in the pairs of images in (c) and (d). The agreement between the image pairs can be quantified by comparing the correlation coefficient and slope calculated using a point to point comparison of the two images. When a sufficient number of frames are averaged, the correlation coefficient and slope will equal 1 if there are no changes in experimental conditions over time. In this example, the correlation coefficient increased from 0.19 to 0.94 and the slope changed from 0.44 to 0.94.

When the results from two separate runs with the same experimental conditions were compared, the averages were similar in the location, shape, and magnitude of the concentration features. Figure 7 shows the average concentration maps obtained for 1000 frames from two separate runs for the configuration with table-like and human-like obstructions.

The effect of obstructions can be seen in Figure 8. The three images show the time-average, fully developed concentration profiles for the three configurations studied: (1) unobstructed, (2) with 5 long 'tables', and (3) with 5 long 'tables' and 12 'humans'. Each image is the average of 1000 frames taken from a single run. These images show that obstructions of the sort that are typically found in rooms can have a significant impact on the average concentration in the measurement plane, even in the absence of thermal plumes. For the configurations studied, the presence of obstructions increases the overall concentration in the measurement plane, increases the peak concentration in the plane, and

shifts the areas of highest concentration. Other configurations of obstructions would almost certainly cause different changes in the concentration profiles and could conceivably even reduce the average concentration in the plane. The important point is not so much the actual concentration profiles, which would vary with the type and location of the obstructions and source, but more the magnitude of the effects seen. When ‘human’ figures were present, videos of the time sequence show dye rising up near the source along the figures and entering the measurement plane near head level. We also see that, when ‘table’ obstructions were present, the dye spreads more below the measurement plane and enters the plane as a plume with a larger cross-section. When computer models are used to predict indoor concentrations, the omission of people and objects in the room can lead to significant errors in the predicted concentration profiles. Incorporating obstructions into predictions is especially challenging for locations where interior configurations change frequently, such as exhibition halls and conference centers.

Figure 9 shows the fluctuation intensity in the measurement plane for the three configurations studied. These images show a shift in both the location and strength of the fluctuation intensity when obstructions were added. The fluctuation intensity increased when ‘tables’ were present, but decreased when ‘humans’ were added along with the tables. Based on visual observation of the flow patterns, the fluctuation intensity decrease with ‘humans’ is due to plume rise along the human figures, which localizes the positions where the plume enters the measurement plane and decreases the temporal variability.

## 7. Conclusions

Water-filled scale models are both accurate and practical for collecting high temporal and spatial resolution experimental data. In this study, we demonstrated their utility for improving our understanding of the concentration distributions arising from sudden contaminant releases. We have shown that the results from a water model can be scaled to a full size air-filled room without a significant loss of the effects of molecular diffusion, small scale eddies, turbulent kinetic energy, or turbulent mass diffusivity. This is true even when there is a significant difference between the Reynolds Numbers for the model and room.

In these experiments, the contaminant concentration within a large, ventilated room does not become well mixed over time during a continuous point source release. Rather a concentration pattern develops which may yield higher concentrations in some areas of the room and lower concentrations in others. A stable time-average concentration is established at any given point, but significant temporal variability occurs. Physical obstructions of the type ordinarily found in rooms, such as tables or people, can significantly alter the concentration profile, maximum concentration, and concentration variability in the breathing plane. This was observed even for our tall room, where the floor level obstructions represent only a small fraction of the overall room volume.

Visualization of indoor airflows using a scale model and LIF techniques can be applied to improve the design of ventilation systems to minimize potential exposures, assist with evacuation and disaster planning, and provide insight into the placement of sensors within a large indoor space. Water-filled scale models are particularly well suited for investigating mechanically driven flow and improving our understanding of pollutant

transport in the indoor environment. They are also a valuable source of high resolution data for use in evaluation of the results from computational fluid dynamics models, as discussed in Finlayson et al. (2003).

## Acknowledgements

This work was supported by the Office of Nonproliferation Research and Engineering, Chemical and Biological National Security Program, of the National Nuclear Security Administration under U.S. Department of Energy Contract No. DE-AC03-76SF00098, and by an Individual Research Grant to DJW from the Natural Sciences and Engineering Research Council of Canada.

## Appendix A: Nomenclature (units)

$A_{\text{inlet}}$	combined cross-sectional area of all supply inlets ( $\text{m}^2$ )
$A_1$	$= 0.56$ , empirical inertial subrange constant in the inertial subrange kinetic energy spectrum function $E_k$
$B_0$	$= 0.6$ , empirical constant for rate of energy transfer through the inertial subrange in isotropic turbulence
$D$	molecular mass diffusivity ( $\text{m}^2 \text{s}^{-1}$ )
$D_t$	turbulent mass diffusivity $D_t \sim u_s L / \text{Sc}_t$ , ( $\text{m}^2 \text{s}^{-1}$ )
$k$	kinetic energy of the turbulence, $(u^2 + v^2 + w^2)/2$ ( $\text{m}^2 \text{s}^{-2}$ )
$k_1$	one-dimensional wavenumber $2\pi f / U_{\text{room}}$ , the normalized fluctuation frequency $f$ , Hz, measured for fluid being convected past a fixed point at mean velocity $U_{\text{room}}$ ( $\text{m}^{-1}$ )
$L_x, L_y, L_z$	integral scales of turbulence in the directions $x$ , $y$ , or $z$ in which a velocity fluctuation component $u$ , $v$ , or $w$ is measured (m)
$L$	$= (L_x^{-1} + L_y^{-1} + L_z^{-1})^{-1}$ , effective isotropic integral length scale of turbulence (m)
$Q_{\text{inlet}}$	total volumetric flow rate through the inlets ( $\text{m}^3 \text{s}^{-1}$ )

$S_{\text{inlet or room}}$	geometric length scale of the inlet or the room (m)
$Sc_t$	turbulent Schmidt number $Sc_t = \nu_t/D_t$
$Sc$	molecular Schmidt number $Sc = \nu/D$
$t_{\text{room}}$	residence time scale of fluid in the room (s)
$t_{\text{inlet}}$	residence time scale of fluid in the inlet jets (s)
$Re_T$	Reynolds number $u_s L/\nu$ of the large scale turbulence that supplies the inertial subrange
$Re_{\text{inlet or room}}$	Reynolds number $US/\nu$ of the mean flow from the supply inlet, or in the room.
$u_s$	$= (u^2 + v^2 + w^2)/3$ effective isotropic velocity scale of the large energetic turbulent eddies $(2k/3)^{1/2}$ ( $\text{ms}^{-1}$ )
$u, v, w$	root mean square turbulence velocity components in x, y, z directions ( $\text{ms}^{-1}$ )
$U_{\text{inlet}}$	mean velocity the inlet supply jets ( $\text{s}^{-1}$ )
$U_{\text{room}}$	mean velocity scale $Q_{\text{inlet}}/V_{\text{room}}^{2/3}$ for the fluid circulation in the room ( $\text{s}^{-1}$ )
$V_{\text{room}}$	room volume ( $\text{m}^3$ )

### Greek Symbols

$\varepsilon$	turbulent energy transfer rate $B_o u_s^3/L$ from larger to smaller eddies in the inertial subrange of the spectrum and the viscous energy dissipation rate at the small eddy end of the spectrum ( $\text{W kg}^{-1}$ , same as $\text{m}^2 \text{s}^{-3}$ )
$\eta$	Kolomorgov length scale of the smallest eddies, $(\nu^3/\varepsilon)^{1/4}$ (m)
$\nu$	kinematic molecular viscosity ( $\text{m}^2 \text{s}^{-1}$ )
$\nu_t$	turbulent eddy viscosity $\nu_t \sim u_s L$ ( $\text{m}^2 \text{s}^{-1}$ )

### Appendix B: Derivation of Scaling Equations

The frequency spectrum of velocity fluctuations (the eddy cascade) can be characterized by two parameters, the Reynolds number ( $Re_L = u_s L/\nu$ ) of the large scale turbulence that supplies the inertial subrange and the scale ratio ( $L/\eta$ ) that sets the range of

scales in the spectrum. Large-scale turbulent field structure depends on the large scale mean and turbulent velocity fields. Model values can be scaled up to equivalent full-scale room values by using length and velocity scales of the mean flow. It is implicitly assumed that if the turbulence velocities and scales are anisotropic, that the degree of turbulence anisotropy remains the same in the scale model and full scale rooms. With this important assumption, we can characterize turbulent velocities, length scales and diffusivities by a single isotropic value, the same in all three component directions, x, y and z.

### *B.1 Loss of Smallest Eddy Sizes in the Scale Model*

At high enough mean flow Reynolds numbers, the classic eddy cascade extends from its largest scale,  $L$ , where the kinetic energy is being produced, through the inertial subrange to the smallest scales, where viscous energy dissipation occurs. A schematic of this classic eddy cascade is shown in Figure 1. In the inertial subrange, the energy supply to the dissipative end of the cascade is set by an energy transfer rate between adjacent eddy sizes,  $\varepsilon = B_0 u_s^3 / L$ . Here, a single velocity and length scale are used with  $u_s^2 = (u^2 + v^2 + w^2)/3$ , and the anisotropy of the turbulence that produces different velocity and length scales in x, y and z is assumed to be constant, so that the ratios of velocity variances  $v^2/u^2$  and  $w^2/u^2$  are the same in model and full scale. Assuming that the dissipation is isotropic, the length scales in the x, y and z directions add as inverses,  $L^{-1} = (L_x^{-1} + L_y^{-1} + L_z^{-1})$ . The energy transfer rate  $\varepsilon$  through the spectrum is equal in magnitude to the rate at which viscous dissipation removes kinetic energy from the small eddy end of the cascade. The velocity scale,  $u_s$ , of the large energetic turbulent eddies is defined as  $u_s = (2k/3)^{1/2}$ , where  $k$  is the kinetic energy of the turbulence. The constant  $B_0$  depends on the precise definition

of  $L$ . Here we take  $L$  to be the integral scale of turbulence in the direction ( $x$ ,  $y$ , or  $z$ ) in which a velocity fluctuation component is measured, resulting in  $B_0 = 0.6$  for isotropic turbulence (see Hinze, 1975). The integral scale can be thought of as the size of the large energetic eddies that contribute most of the kinetic energy of turbulence. The smallest eddies have a size  $\eta = (\nu^3/\epsilon)^{1/4}$ , the Kolomorgov length scale. The size of the smallest eddy is determined by the turbulent kinetic energy dissipation rate,  $\epsilon$ , and by the kinematic molecular viscosity,  $\nu$ , available to do the dissipating.

Lowering the Reynolds number increases the size of the smallest eddies in the

$$\frac{L_{room,full}}{\eta_{room,full}} = B_0^{1/4} \text{Re}_{T,room,full}^{3/4}$$

system. The magnitude of this increase can be estimated by the ratio of large to small eddy sizes, found by inserting the large eddy definition of  $\epsilon$  in the definition of  $\eta$ ,

where the turbulence Reynolds number  $\text{Re}_T$  is defined in terms of the turbulence velocity  $u_s$

$$\text{Re}_{T,room,full} = \frac{u_{s,room,full} L_{room,full}}{\nu_{air}}$$

and the large eddy scale  $L$ ,

A similar scale ratio  $L_{room,model} / \eta_{room,model}$  can be written for the scale model, with the

$$\text{Re}_{T,room,model} = \frac{u_{s,room,model} L_{room,model}}{\nu_{water}}$$

turbulence Reynolds number,

The size of the most energetic eddies,  $L_{room}$ , depends on the physical dimensions of the enclosure and the intensity of turbulence. Based on observation of the video images,

we roughly estimated the most energetic Eulerian fixed frame eddies (passing a fixed point in space) to be about  $L_{\text{room}} \sim 0.1 S_{\text{room}}$ . Note that an observer looking at a full field image sees the Lagrangian eddy scale moving with the flow, rather than the Eulerian scale at a fixed point. Karnik and Tavoularis (1990) found conversion constants between the Lagrangian and Eulerian time scales of 1.36 to 2.00 at moderate Reynolds number. Based on measurements of atmospheric turbulence, Hanna (1981) reported a time conversion factor of 3.84 at high Reynolds number in wind shear flow near a surface (the ground). We made a rough conversion of the observed Lagrangian length scale to the Eulerian fixed frame of reference by multiplying the Lagrangian scale by  $2.5u_s/U_{\text{room}}$ .

To determine the turbulence velocity scale,  $u_s$ , the mean kinetic energy dissipated within the supply jet must be estimated. We assumed that half the mean kinetic energy flux in the supply jets was dissipated close to the inlets within the supply jets and the other half dissipated in the room. This produces a turbulence velocity scale of  $u_s \sim 0.1 U_{\text{inlet}}$ , the inlet supply velocity. Fortunately,  $u_s$  isn't very sensitive to the jet dissipation fraction chosen, since it is proportional to the 1/3 power of the kinetic energy dissipated in the room. For example, if only 10% of the energy was dissipated in the jet,  $u_s$  would only increase by about 20%.

Using these values of  $u_s$  and  $L$ , the turbulence Reynolds numbers were  $Re_{T,\text{room,full}} = 2570$ , and  $Re_{T,\text{room,model}} = 500$  for a model flow of  $Q_{\text{inlet,model}} = 28$  lpm (20% of the flow rate needed to match model and full scale Reynolds numbers). These Reynolds numbers yield a scale range of  $L_{\text{room,full}}/\eta_{\text{room,full}} = 410$  and  $L_{\text{room,model}}/\eta_{\text{room,model}} = 120$ , for the full-scale and model rooms respectively. From this, the smallest eddies in the full scale room air were calculated to be  $\eta_{\text{room,full}} = 0.38$  cm and the smallest eddies in the water model were

$\eta_{\text{room,model}} = 0.032$  cm. Multiplying by 30 to scale up the water model eddies to their equivalent full scale size gives a value of  $\eta_{\text{room,scaleup}} = 0.97$  cm. Velocity eddies between the actual Kolomorgov scale of 0.38 cm in the full scale room air and the scaled-up model value of 0.97 cm were not simulated in the water experiments.

## B.2 Loss of Turbulence Kinetic Energy in the Scale Model

The lower turbulence Reynolds number in the water model cuts off the scaled-up velocity fluctuation spectrum of the scaling velocity,  $u_s^2$ , at lower wave numbers than occur in the full-scale room. The one-dimensional wave number  $k_1 = 2\pi f / U_{\text{room}}$ , cycles  $\text{m}^{-1}$ , is the normalized inverse wavelength of fluctuation frequency  $f$ ,  $\text{s}^{-1}$ , measured for fluid being convected past a fixed point at mean velocity  $U_{\text{room}}$ . For illustration, consider a sharp viscous dissipation cutoff at  $k_1 = \eta^{-1}$ . The lost kinetic energy in the scaled up water model is

$$u_{s \text{ room,scaleup}}^2 = u_{s \text{ room,fullscale}}^2 - \int_{1/\eta_{\text{room,scaleup}}}^{1/\eta_{\text{room,full}}} \frac{5}{3} A_1 \epsilon^{2/3} k_1^{-5/2} dk_1$$

The integrand is the one-dimensional velocity spectrum of the scaling velocity,  $u_s^2$ , in the inertial subrange, where  $A_1 = 0.56$  is an empirical inertial subrange constant (see Hinze, 1975). Carrying out the integration and using the inertial subrange energy transfer rate  $\epsilon = B_0 u_s^3 / L$  for the full scale room,

$$\frac{u_{s\text{ room,scaleup}}^2}{u_{s\text{ room,full}}^2} = 1 - 1.1 \text{Re}_{T,\text{room,full}}^{-1/2} \left[ \left( \frac{\eta_{\text{room,scaleup}}}{\eta_{\text{room,full}}} \right)^{2/3} - 1 \right]$$

With  $\text{Re}_{T,\text{room,full}} = 2570$ ,  $\eta_{\text{room,full}} = 0.38 \text{ cm}$  and  $\eta_{\text{room,scaleup}} = 0.97 \text{ cm}$ , this yields

$u_{s\text{ room,scaleup}}^2/u_{s\text{ room,full}}^2 = 0.98$ , so only 2% of the turbulence kinetic energy is lost in the water model. Taking the square root of this energy ratio shows that only 1% of the turbulent scaling velocity  $u_s$  is lost in scaling up from the water model. However, this small loss in velocity scale may not be equally distributed over all three components  $u$ ,  $v$ , and  $w$  of the turbulent velocity. The model flow may be more or less anisotropic than the full-scale flow, and this change in flow anisotropy could have a significant effect on turbulent diffusivities in the  $x$ ,  $y$  and  $z$  directions.

### B.3 Loss of Turbulent Mass Diffusivity $D_t$ in the Scale Model

Assuming the turbulence is isotropic, with the same turbulent diffusivities of momentum and mass in all three component directions,  $x$ ,  $y$ , and  $z$ , the turbulent eddy viscosity,  $\nu_t$ , is proportional to the product of the turbulent scaling velocity,  $u_s$ , and the length scale,  $L$ , of the large energetic eddies. The relation  $\nu_t \sim u_s L$ , can be expressed in terms of the kinetic energy transfer rate  $\varepsilon = B_o u_s^3 / L$  through the inertial subrange by using  $L = B_o u_s^3 / \varepsilon$  so that  $\nu_t \sim u_s^4 / \varepsilon$ . Assuming the same value of the turbulent Schmidt number  $\text{Sc}_t = \nu_t / D_t$  in model and full scale,  $D_t \sim u_s^4 / \varepsilon$ . Then, assuming that the water model properly simulates the energy transfer rate  $\varepsilon = B_o u_s^3 / L$  through the inertial subrange, we expect that  $\varepsilon_{\text{room,scaleup}} = \varepsilon_{\text{room,full}}$ , and the ratio of scaled-up isotropic mass diffusivity to the

isotropic diffusivity in the full scale room should just be the ratio of  $u_s^4$  of the scaled-up model to the full-scale room, so that

$$\frac{D_{t,room,scaleup}}{D_{t,room,full}} = \left[ 1 - 1.1 \text{Re}_{T,room,full}^{-1/2} \left[ \left( \frac{\eta_{room,scaleup}}{\eta_{room,full}} \right)^{2/3} - 1 \right] \right]^2$$

For our water filled 30:1 scale model operating at 28 liters per minute, this equation gives a value of 0.96 for the ratio of scaled-up to actual room turbulent mass diffusivities. Again, we have no way to estimate the effect of changing anisotropy of the flow on the turbulent mass diffusivities  $D_{t,x}$ ,  $D_{t,y}$  and  $D_{t,z}$  in the x, y and z directions

## References

- Arcoumanis C, McGuirk JJ, Palma JMLM (1990) On the use of fluorescent dyes for concentration measurements in water flows, *Experiments in Fluids*, **10**, pp 177-180.
- Bain JM (2001) Laboratory airflow studies in a scale model subway station. M.S. Thesis, University of Illinois at Urbana-Champaign.
- Baughman AV, Gadgil AJ, Nazaroff WW (1994) Mixing of a point source pollutant by natural convection flow within a room, *Indoor Air*, **4**, pp 114-122.
- Crimaldi JP, Koseff JR (2001) High-resolution measurements of the spatial and temporal scalar structure of a turbulent plume, *Experiments in Fluids*, **31**, pp 90-102.
- Drescher AC, Lobascio C, Gadgil AJ, Nazaroff WW (1995) Mixing of a point source indoor pollutant by forced convection, *Indoor Air*, **5**, pp 204-214.
- Finlayson EU, Gadgil AJ, Thatcher TL (2002) Pollutant dispersion in a large indoor space: Computational Fluid Dynamics (CFD) predictions and comparison with a scale model experiment for isothermal flow. Lawrence Berkeley National Laboratory Report, LBNL-50105, Berkeley, CA.

- Fischer ML, Price PN, Thatcher TL, Schwalbe CA, Craig MJ, Wood EE, Sextro RG, and Gadgil AJ (2001) Rapid measurements and mapping of tracer gas concentrations in a large indoor space, *Atmospheric Environment*, **35**, pp 2837-2844.
- Freymuth P (1993) Flow visualization in fluid mechanics, *Review Scientific Instrumentation* **64**, pp 1-18.
- Gavelli F, Kiger K (2000) High-resolution boron dilution measurements using laser induced fluorescence (LIF), *Nuclear Engineering and Design*, **195**, pp 13-25.
- Hanna S (1981) Lagrangian and Eulerian time-scale relations in the daytime boundary layer, *Journal of Applied Meteorology* **20**, 242-249
- Hesslink L (1988) Digital image processing in flow visualization, *Annual Review Fluid Mechanics*, **20**, pp 421-485.
- Hinze JO (1975) *Turbulence, 2<sup>nd</sup> Edition*, McGraw Hill, New York, pp 223-229, 245, and 255.
- Huber AH, Arya SP, Rajala SA, and Borek JW (1991) Preliminary study of video images of smoke dispersion in the near wake of a model building, *Atmospheric Environment*, **25A**, pp 1199-1209.
- Hunt GR, Linden PF (1999) The fluid mechanics of natural ventilation - displacement ventilation by buoyancy-driven flows assisted by wind, *Building and Environment*, **34**, pp 707-720.
- Hunt GR, Cooper P, Linden PF (2001). Thermal stratification produced by plumes and jets in enclosed spaces, *Building and Environment*, **36**, pp 871-882.
- Karnik U, Tavoularis S (1990) Lagrangian correlations and scales in uniformly sheared turbulence, *Physics of Fluids*, **2**, pp 587-591.
- Koochesfahani MM, Dimotakis PE (1985) Laser-induced fluorescence measurements of mixed fluid concentration in a liquid plane shear layer, *American Institute of Aeronautics and Astronautics*, **23**, pp 1700-1707.
- Lemoine F, Antoine M, Wolff M, Lebouche M (1998) Mass transfer properties in a grid generated turbulent flow: some experimental investigations about the concept of turbulent diffusivity, *International Journal of Heat and Mass Transfer*, **41**, pp 2287-2295.
- Tennekes H, Lumley JO (1972) *A First Course in Turbulence*, MIT Press, Cambridge, MA pp 8-22, 67-68.
- Shlien DJ (1988) Instantaneous concentration field measurement technique from flow visualization photographs, *Experiments in Fluids*, **6**, pp 541-546.
- Unger DR, Muzzio FJ (1999) Laser-induced fluorescence technique for the quantification of mixing in impinging jets, *American Institute of Chemical Engineering Journal*, **45**, pp 2477-2486.

United States Department of Transportation (1975) *Subway Environmental Design Handbook, Volume 1: Principles and Applications*, 2nd ed, GPO, Washington, D.C. Appendices A, B.

Walker DA (1987) A fluorescence technique for measurement of concentration in mixing liquids, *Journal of Physics Series E: Scientific Instruments*, **20**, pp 86-94.

Wilson DJ (1995) *Concentration Fluctuations and Averaging Time in Vapor Clouds*, Center for Chemical Process Safety, American Institute of Chemical Engineers, New York

Table 1a: Ratio between model and full scale characteristics for perfect Reynolds number matching.

Medium	Length Ratio	Flowrate Ratio	Time Ratio	Volume changes per hour Ratio
water	1:10	117:1	9:1	9:1
	1:30	350:1	77:1	77:1
air	1:4	4:1	16:1	16:1
	1:10	10:1	100:1	100:1
	1:30	30:1	900:1	900:1

Table 1b: Properties of the full scale system and several model configurations when the model/full time scale ratio is set at 15:1.

Medium	Model: Full Scale	Volume	Volume	Inlet	Reynolds	$\eta$ (cm)	$\eta$ (cm)	Kinetic	Mass
	Length Ratio	(m <sup>3</sup> )	Changes	Velocity	Number		scaled-up	Energy	Diffusivity
			per Hour	(m/s)				Ratio	Ratio
Full scale air	-	750	4	0.44	2861	0.264	-	-	-
water	10	0.75	60	0.66	5007	0.017	0.17	1.01	1.01
	30	0.028	60	0.22	556	0.030	0.90	0.98	0.96
air	4	11.7	60	1.65	2683	0.069	0.28	1.00	1.00
	10	0.75	60	0.66	429	0.109	1.09	0.97	0.93
	30	0.028	60	0.22	48	0.190	5.69	0.64	0.41

Figure 1: A schematic of the classic turbulent eddy cascade which describes the energy transport through a range of turbulent eddy sizes. The eddy cascade extends from the largest scale eddies, where the kinetic energy is being produced, through the inertial subrange where there is no production or dissipation, to the smallest scales, where viscous energy dissipation occurs.

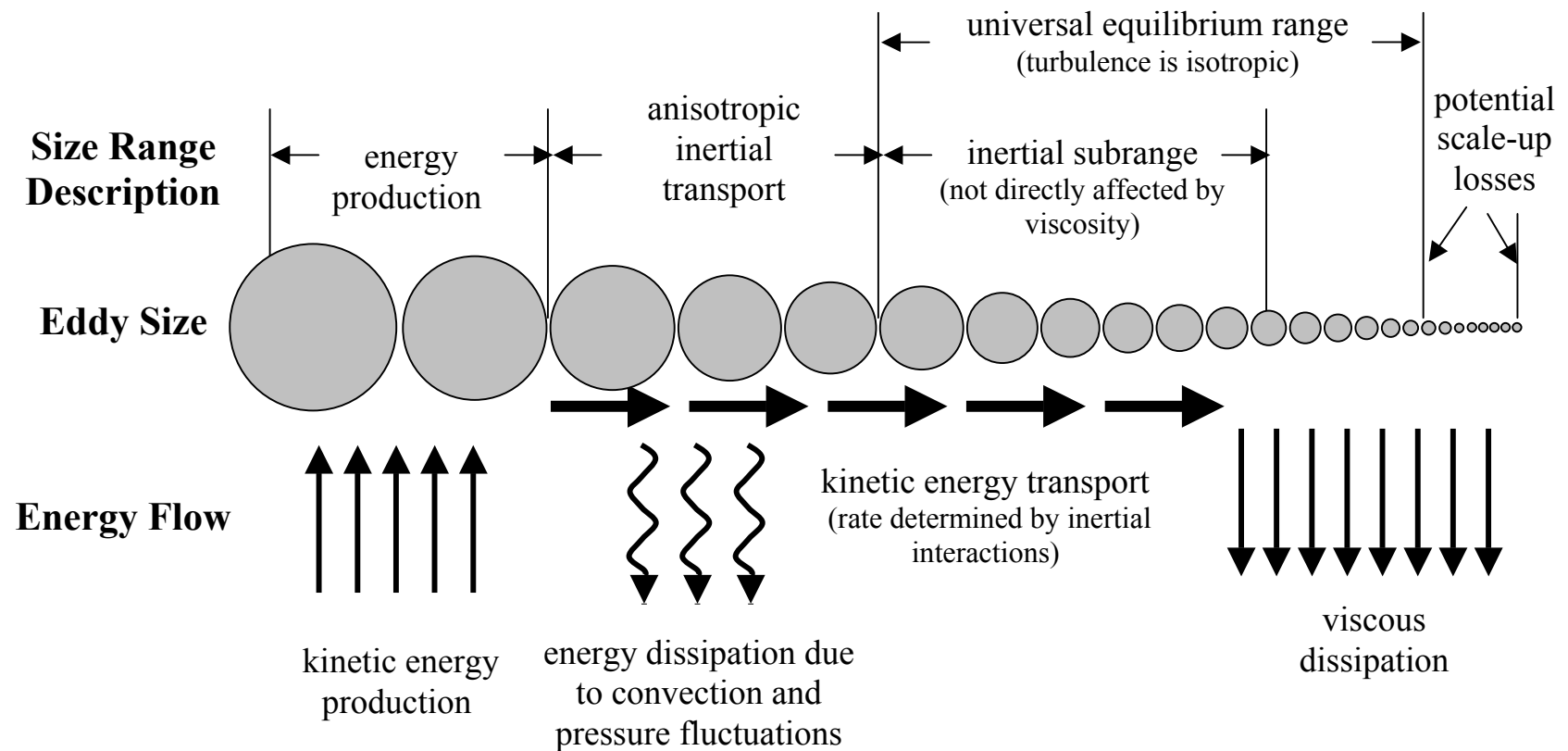


Figure 2: Schematic view of the water scale model.

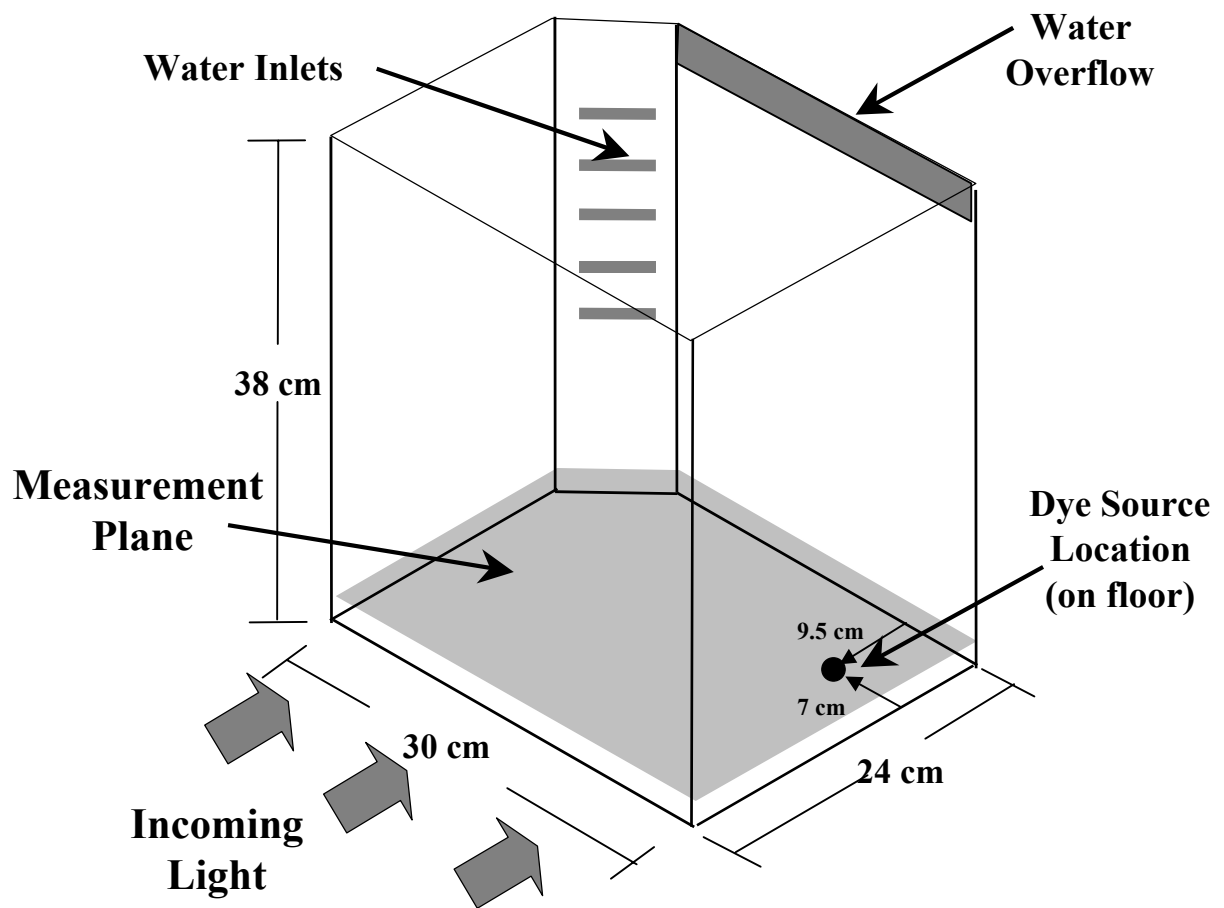


Figure 3: Scale model obstructions simulating “people” and “tables”.

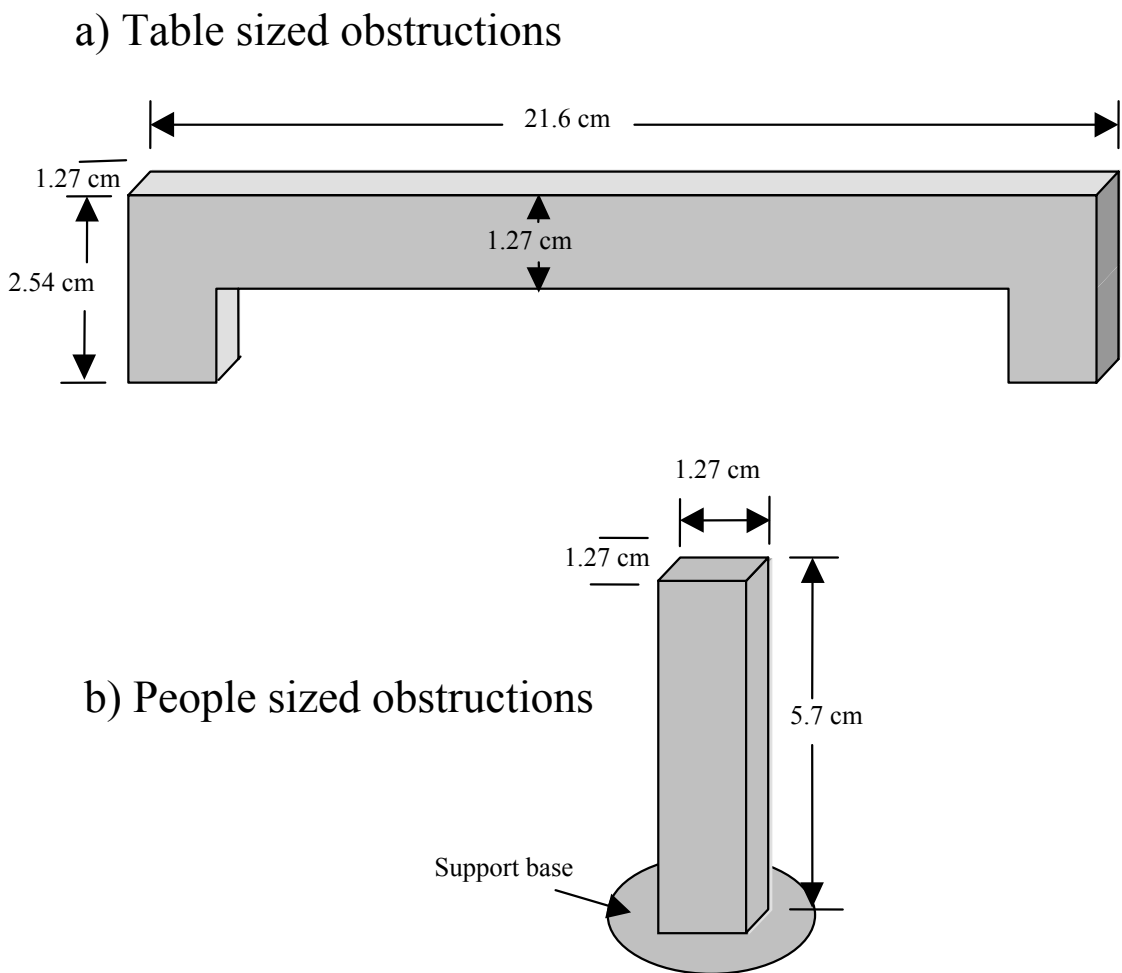


Figure 4: Overhead view of the model showing locations of the dye source and the movable obstructions.

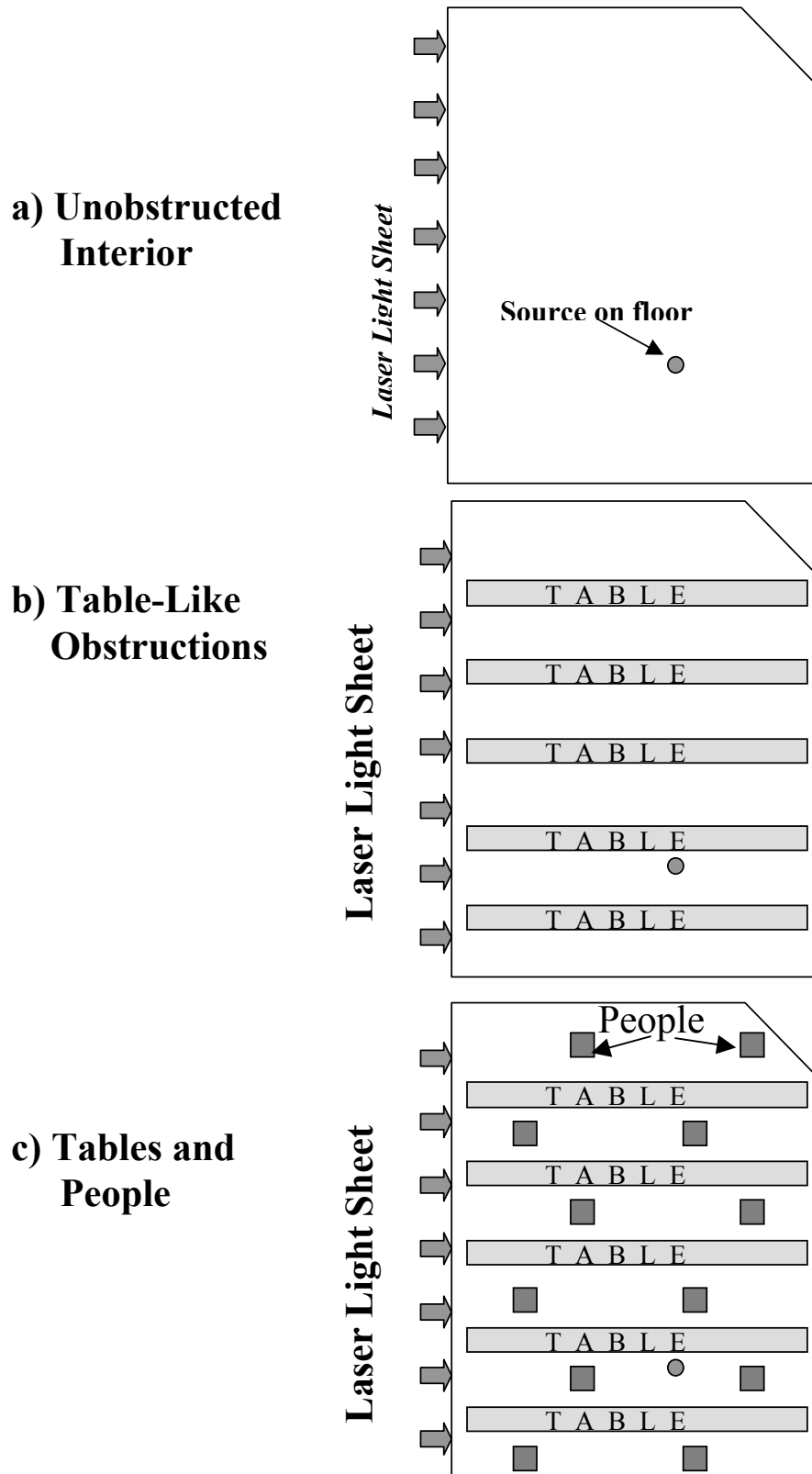


Figure 5: Time series of the average concentration profiles (from 19 independent runs) in the measurement plane for the unobstructed model. Times are the elapsed time after initiating dye injection. Darker shading indicates higher concentrations.

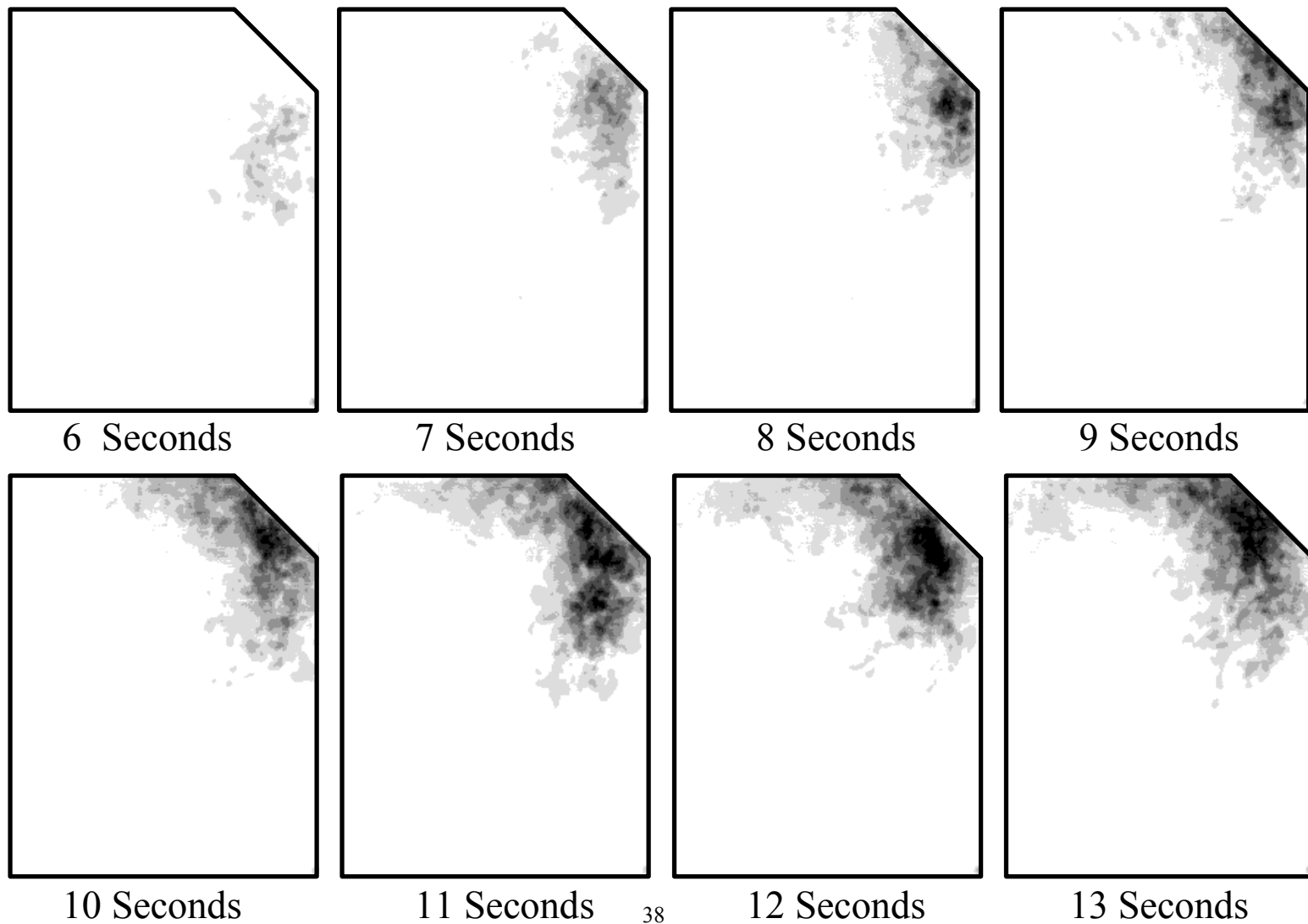


Figure 6: Full developed concentration profiles for the unobstructed model. The number of instantaneous images used to obtain the average was increased from 1 to 200.  $r^2$  and slope based on point to point comparison of image pairs. All images used in the averages were taken from a single experimental run. Darker shading indicates higher concentrations.

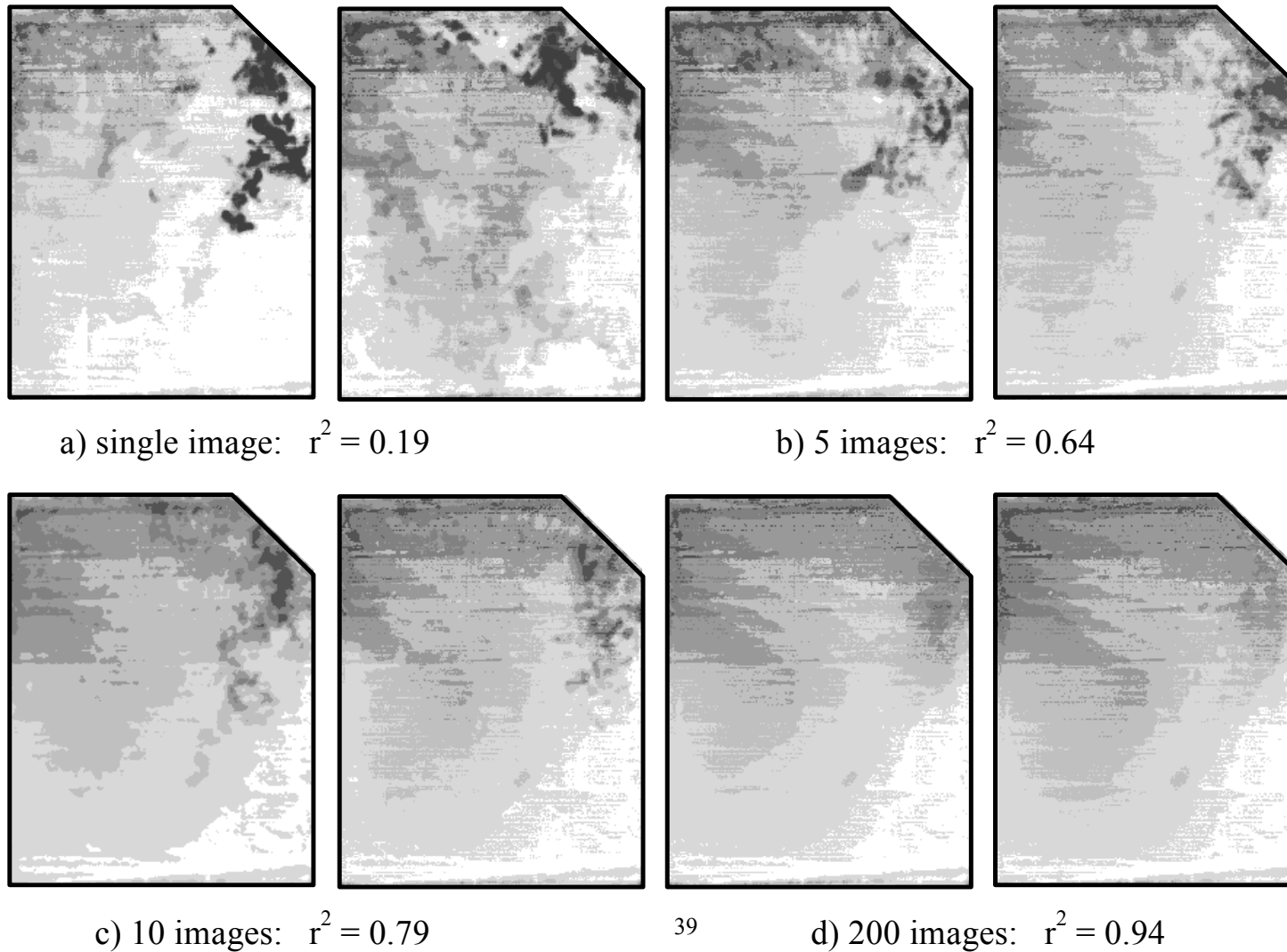


Figure 7: Comparison of the time-averages of 1000 frames from fully developed concentration profiles in two separate experiments where 'table' and 'human' shaped obstructions were present and experimental conditions were duplicated as closely as possible. The concentration within the darkest contour is approximately ten times that in the lightest contour. The correlation coefficient between the two images is 0.91

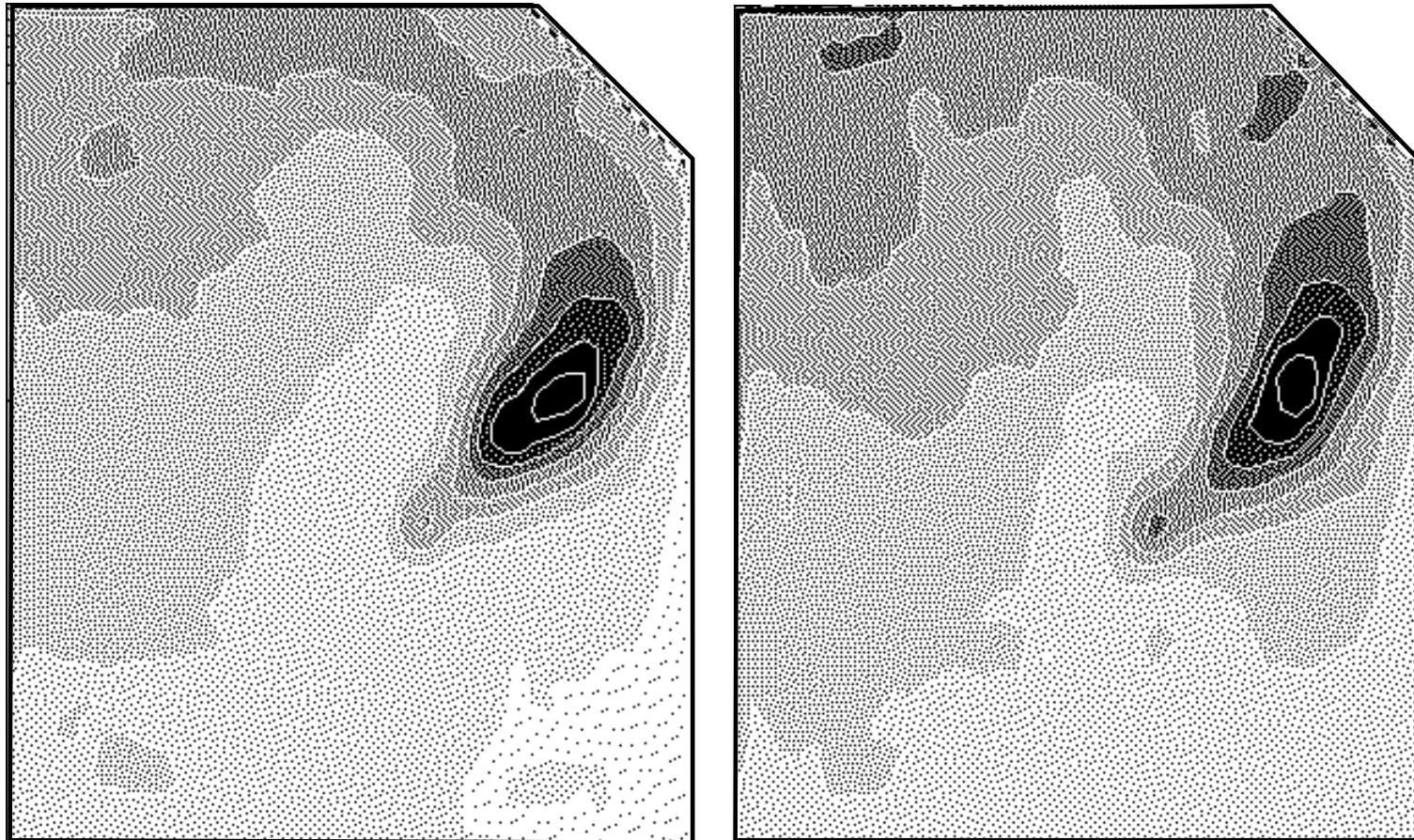


Figure 8: Time-averages of 1000 images from fully developed concentration profiles with three different levels of obstruction of the floor of the model. Concentrations are normalized by the average, fully-developed outlet concentration. The concentration within the darkest contour is approximately ten times that in the lightest contour.

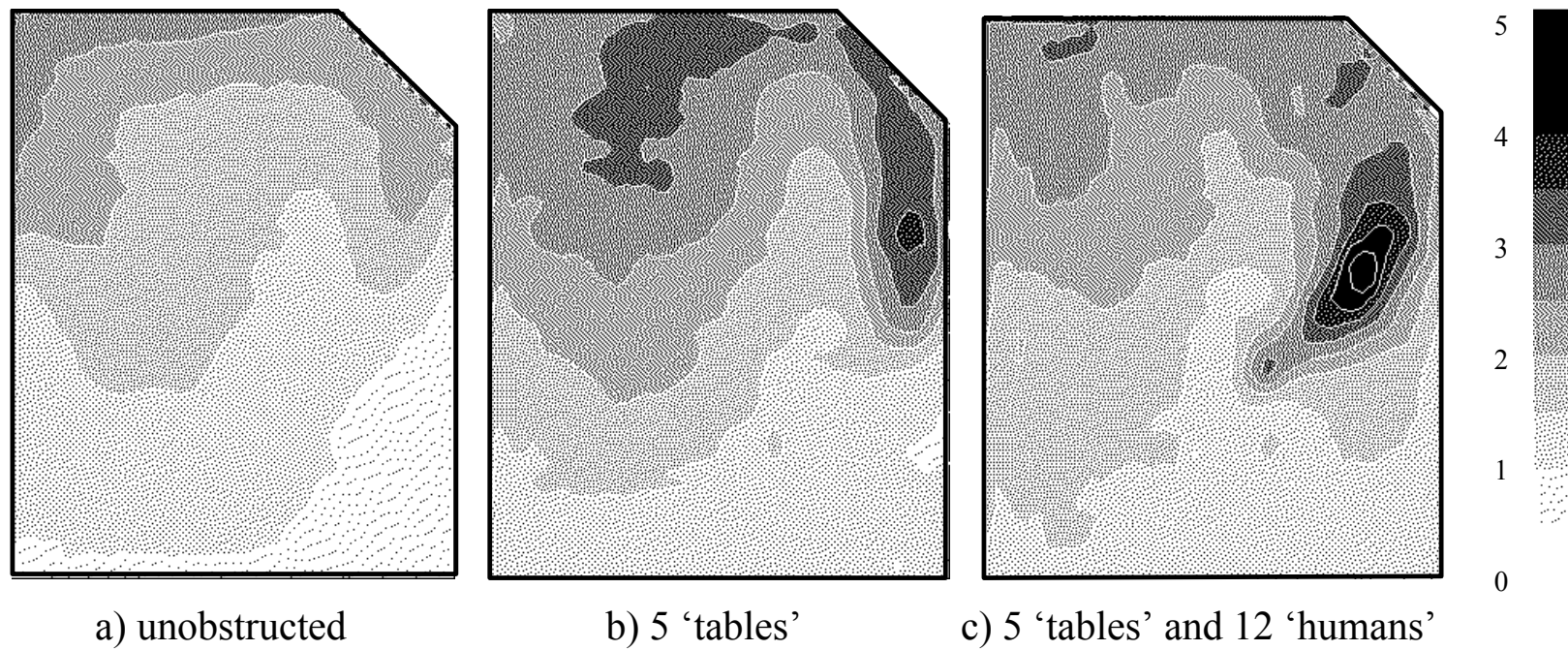


Figure 9: Time-average fluctuation intensity of 1000 images about the fully developed concentration profiles for three different levels of obstructions on the floor of the model. The fluctuation intensity is defined as the standard deviation at each point divided by the average concentration at the same point.

